ADVANCED ENERGY MATERIALS

Supporting Information

for *Adv. Energy Mater.,* DOI: 10.1002/aenm.201400216

Universal Design Principles for Cascade Heterojunction Solar Cells with High Fill Factors and Internal Quantum Efficiencies Approaching 100%

*Adam Barito, Matthew E. Sykes, Bingyuan Huang, David Bilby, Bradley Frieberg, Jinsang Kim, Peter F. Green, and Max Shtein**

Supporting Information

Universal design principles for cascade heterojunction solar cells with high fill factors and internal quantum efficiencies approaching 100%

*Adam Barito, Matthew E. Sykes, Bingyuan Huang, David Bilby, Bradley Frieberg, Jinsang Kim, Peter F. Green, and Max Shtein**

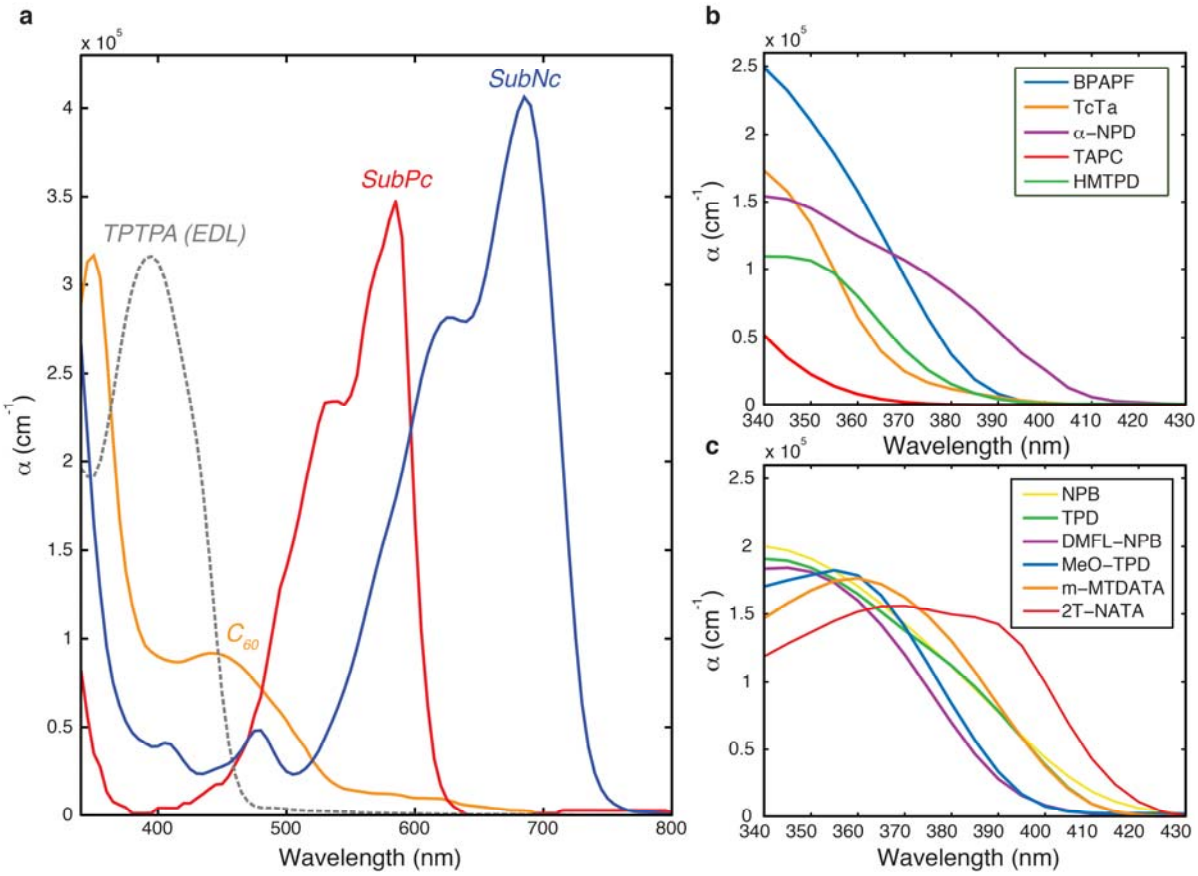

Figure S1. Absorption coefficients of active materials used in this study, as determined by variable angle spectroscopic ellipsometry. Spectra are shown for a) absorbing energy harvesting layers SubPc, SubNc (at normal incidence), C_{60}, and TPTPA EDL; b) EDLs BPAPF, TcTa, α-NPD, TAPC, and HMTPD; and c) EDLs NPB, TPD, DMFL-NPB, MeO-TPD, m-MTDATA, and 2T-NATA.

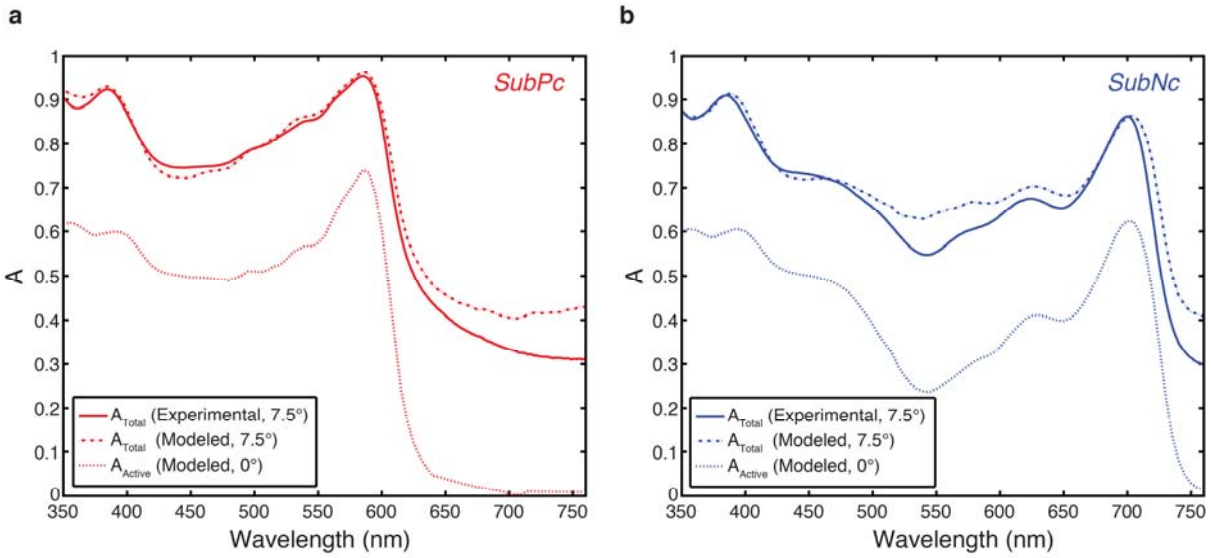

Figure S2. Experimental and modeled absorption spectra of a) SubPc/C_{60} and b) SubNc/C_{60} CHJ devices. Total absorption of the device stack was measured and modeled at an incidence angle of 7.5°. Active layer absorption (absorption in only the interlayer and C_{60} layers) was modeled at normal incidence and used in calculating the IQE of device stacks.

#

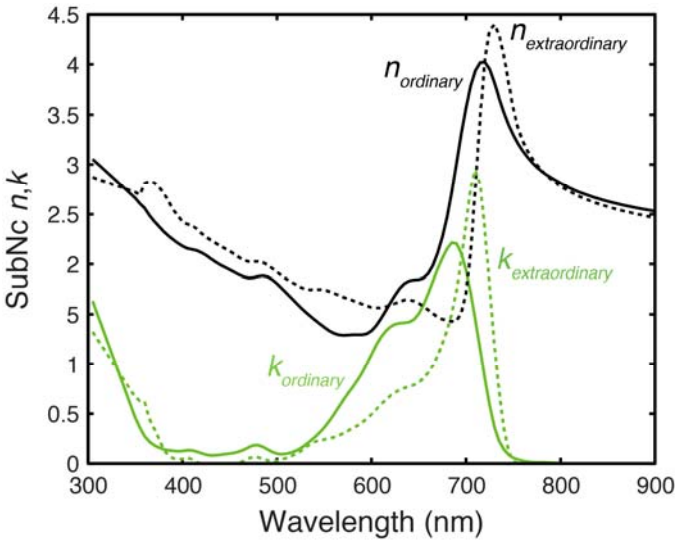

Figure S3. Ordinary and extraordinary complex refractive indices, ($\tilde{n} = n + ik$) of SubNc, measured and fit by variable angle spectroscopic ellipsometry with consideration for anisotropy. Both n and k are significantly different from what has been previously reported in literature[1] but provided much more physically reasonable fits to modeled absorption of neat films and device stacks.

1. Onsager Braun Modeling

The voltage dependence of photocurrent in a SubPc/C_{60} SHJ device was simulated using the Onsager-Braun (OB) model,[2] whereby bound polaron pairs (PPs) at the heterojunction are treated as Coulombically-bound charges with a fixed separation distance (a_0). The temperature-dependent, field-assisted dissociation rate of PPs (k_{PPd}) is described by:

$$k_{PPd} = \frac{3q}{4\pi\varepsilon_r\varepsilon_0 a_0^3}\exp\left(\frac{-E_B}{k_b T}\right)\cdot\frac{J\left[2\sqrt{2}\left(-b\right)^{1/2}\right]}{\sqrt{2}\left(-b\right)^{1/2}} \quad \text{(S1)}$$

where q is the electron charge, $\langle\mu\rangle$ = 1x10^{-4} cm^2/V-s is the average charge mobility about the interface, ε_r = 4 is the relative permittivity to the vacuum permittivity (ε_0), $E_B = q^2/\left(4\pi\varepsilon_r\varepsilon_0 a_0\right)$ is the PP binding energy, $k_B T$ is the thermal energy, and J is the first-order Bessel function. The term b in (S1) is defined as $b = q^3\left(V_a - V_{bi}\right)/\left(8\pi d\varepsilon_r\varepsilon_0 k_b^2 T^2\right)$, where V_{bi} is the built-in voltage defined by the difference in Fermi levels in the organic layers adjacent to the contacts at zero bias, V_a is the applied bias voltage, and d is the thickness of the active layers. Here we assume the net field in the active layers is constant as a function of position, which is reasonable considering charge injection from the contacts is minimal below V_{bi}. Furthermore the study of photocurrent alone (and not total current) allows one to neglect the effects of charge injection and transport through the active layers and focus solely on the dynamics of the heterojunction. Along with a_0 and V_{bi}, the recombination rate (k_r) of the bound charges across the interface is then used as a fitting parameter, and the overall PP dissociation efficiency at the heterojunction can be defined as:

$$\eta_{PPd} = \frac{k_{PPd}}{k_{PPd} + k_r} \quad \text{(S2)}$$

Figure S4 shows the normalized photocurrent for a SubPc/C_{60} junction measured under simulated AM1.5 illumination (100 mW/cm^2). As can be seen, the OB model produces a

much higher FF than what is measured experimentally in such devices. Renshaw *et al.* have shown previously that photoconductivity (S_{pc}) must be accounted for to properly describe the photocurrent in OPVs (in particular SubPc/C_{60}) and resolve this discrepancy.[3] The total normalized photocurrent can be described by:

$$\frac{J_{ph}(V_a)}{J_{sc}} = \frac{S_{pc}}{J_{sc}} \cdot \left(V_a - V_{bi}\right) - f_{jxn} \cdot \eta_{PPd} \qquad \text{(S3)}$$

where $f_{jxn} = 1 - \frac{S_{pc} \cdot V_{bi}}{J_{sc}}$ is the fraction of photocurrent produced at short-circuit conditions from the heterojunction and not from bulk dissociation. From the slope of the photocurrent curves in reverse bias we obtained S_{pc} values of 0.55 mA/cm^2-V and 0.65 mA/cm^2-V for SubPc/C_{60} and SubNc/C_{60} devices, respectively. When S_{pc} was included in (S3), the experimental and modeled photocurrents were closely matched. For SubPc/C_{60}, values of 0.95 V, 1.22 nm, and 10^8 Hz were used for V_{bi}, a_0, and k_r, respectively (the 1.22 nm a_0 corresponds to a 0.304 eV E_B). For SubNc/C_{60}, values of 0.65 V, 1.16 nm, and 10^8 Hz were used for V_{bi}, a_0, and k_r, respectively (the 1.16 nm a_0 corresponds to a 0.319 eV E_B). Having determined the parameters for the SubPc/C_{60} SHJ device, it was then possible to solely vary the PP separation distance (and thus binding energy, E_B) to observe its effect on the maximum power point voltage under realistic conditions (Figure 3). We note that our fitted values for SubPc/C_{60} are in close agreement with those reported in literature.[4]

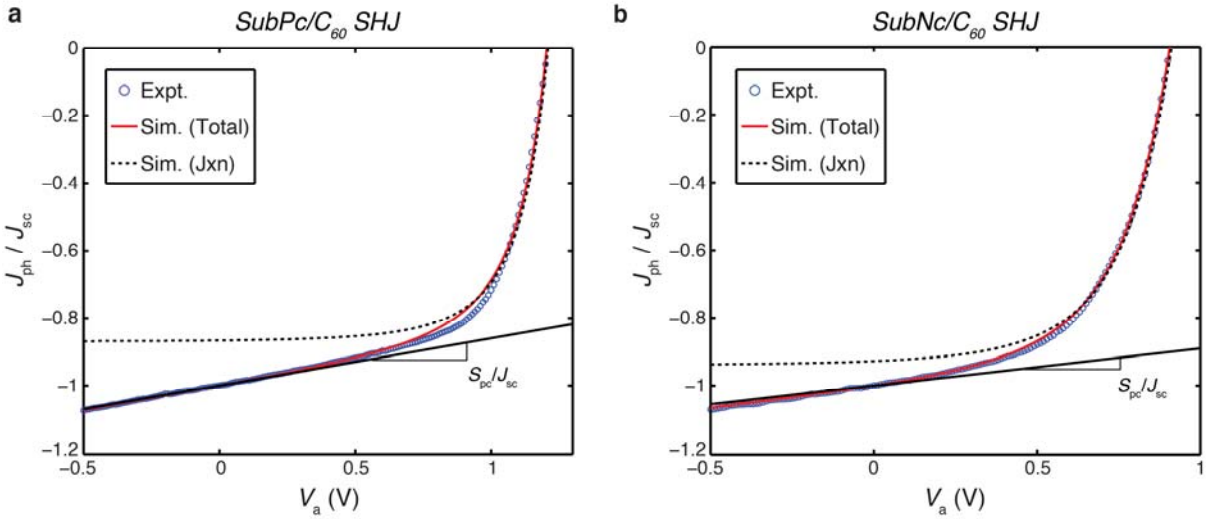

Figure S4. Normalized photocurrent versus applied bias for a) SubPc/C_{60} and b) SubNc/C_{60} SHJ devices fitted to the OB model. Experimental data is shown (blue circles) to be in excellent agreement with the overall device fitting (solid red line) comprising contributions from dissociation at the heterojunction (dashed black line) and photoconductivity (solid black line).

2. Effect of EDL Mobility on CHJ Performance

To determine any effects of EDL mobility on the V_{MPP} of CHJ devices, we used time-of-flight methods to measure the hole mobility of select EDL materials (**Figure S5**a). The remaining mobilities were taken from time-of-flight measurements reported in literature.[5-8] In Figure S5b, we plot the zero-field hole mobilities ($\mu_{h,0}$) of each EDL material versus its HOMO level energy; from this plot, there is a noticeable trend between $\mu_{h,0}$ and the HOMO level. HOMO levels and mobility parameters are provided in **Table S1**. Assuming a Poole-Frenkel dependence of the carrier mobility on electric field, [9] the mobility can be expressed as:

$$\mu_h(E) = \mu_{h,0} \exp(\gamma E^{1/2}) \quad \text{(S4)}$$

where $\mu_{h,0}$ is the zero-field hole mobility, γ is the field activation parameter, and E is the applied electric field.

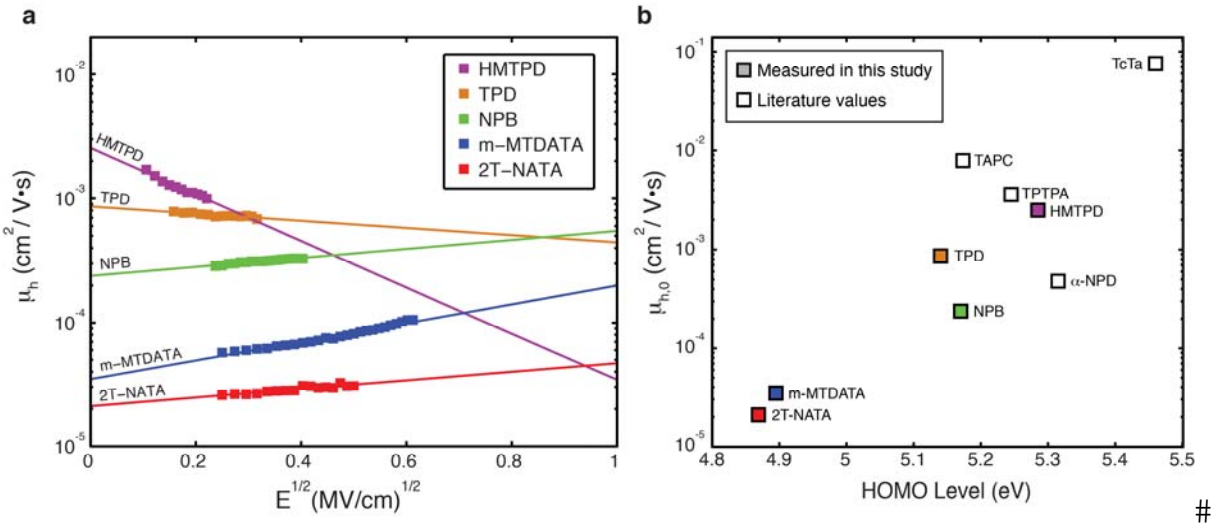

Figure S5. a) Field-dependent hole mobilities of EDL materials measured via time-of-flight methods. b) Zero-field hole mobilities of EDL materials versus HOMO energy level. Colored squares were measured in this study and white squares are (time-of-flight) values taken from literature.

Since both μ_h and the introduced hole injection barrier correlate with ΔE_{HOMO}, we varied EDL thickness for each device set from 5 nm to 10 nm to deconvolve any effects the two properties may have on device performance. Because the injection barrier remains constant regardless of EDL thickness, any changes in performance versus thickness could be attributed to mobility differences in the EDL layer. The normalized V_{MPP} for all CHJ devices can be seen in **Figure S6**a. While the EDL thickness variation introduces an additional spread to the data set, (6) still provides a good overall fit. Furthermore, as can be seen from Figure S6b, there is no clear trend in V_{MPP} as a function of EDL thickness. In fact, some CHJ devices experience an *increase* in V_{MPP} with a thicker EDL layer. While the physical reasons for variations in CHJ performance versus EDL thickness warrant further investigation, they are outside the scope of this study. By varying EDL thickness with no clear trend for changes in V_{MPP}, we conclude that any effects due to changes in mobility are secondary and much smaller than those due to the introduced injection barrier with energy of ΔE_{HOMO}.

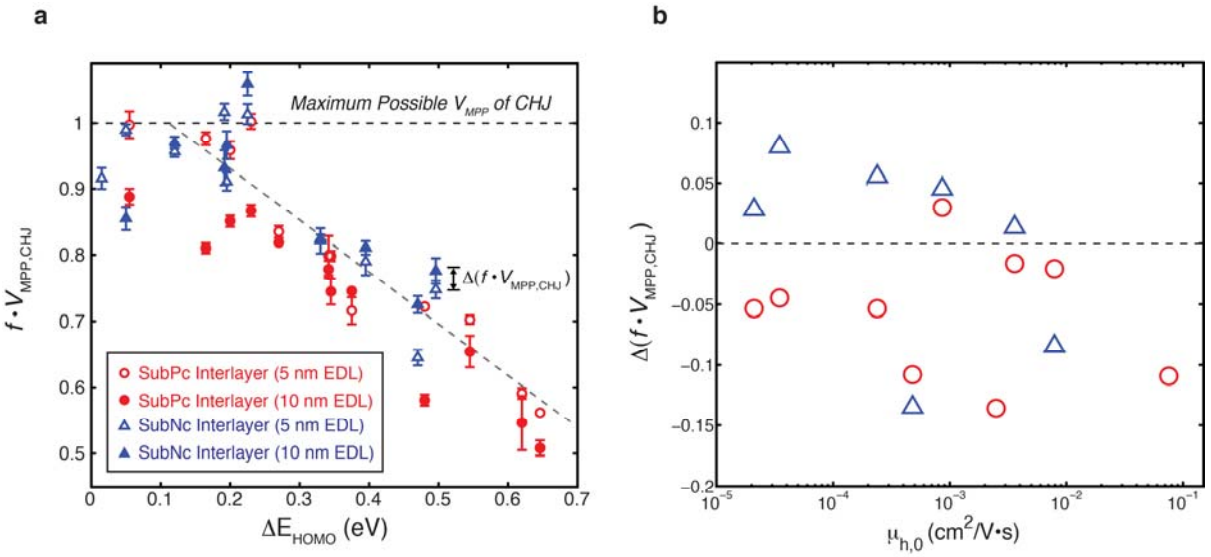

Figure S6. a) A plot of each CHJ V_{MPP} normalized by the minimum V_{MPP} of its constituent subjunctions versus ΔE_{HOMO} (the energy offset between the HOMO levels of the EDL and the interlayer). EDL thicknesses of 5 and 10 nm for both interlayers are shown. b) The difference in normalized V_{MPP} for CHJs with 5 nm and 10 nm EDL thicknesses vs. the zero-field hole mobility of each EDL material. Because there is no clear dependence of V_{MPP} on EDL thickness, we conclude that any changes in CHJ V_{MPP} due to EDL material variation are due primarily to the introduced injection barrier with energy of ΔE_{HOMO}, with effects of mobility variation either negligible or secondary.

Table S1. Mobility parameters for all EDL materials, as determined by time-of-flight measurements. Mobility values taken from literature are noted. All other mobility values and HOMO levels were measured in this study.

Material	HOMO Level (eV)	$\mu_{h,0}$ ($cm^2 V^{-1} s^{-1}$)	γ $(cm V^{-1})^{1/2}$	Source
TcTa	5.46	7.56E-02	5.62E-04	[5]
BPAPF	5.35	-	-	-
α-NPD	5.32	4.80E-04	5.30E-04	[6]
HMTPD	5.29	2.50E-03	-4.30E-03	This study
TPTPA	5.25	3.60E-03	2.90E-03	[7]
TAPC	5.17	7.90E-03	8.81E-04	[8]
NPB	5.17	2.39E-04	8.30E-04	This study
TPD	5.14	8.622E-04	-6.632E-04	This study
DMFL-NPB	5.04	-	-	-
MeO-TPD	4.97	-	-	-
m-MTDATA	4.90	3.478E-05	1.700E-03	This study
2T-NATA	4.87	2.100E-05	8.028E-04	This study

3. EQE of CHJ Devices

In SHJ devices, the EQE is determined by the product of the efficiencies for each individual energy transfer step in the photocurrent generation process:

$$\mathrm{EQE}(\lambda) = \eta_{\mathrm{Abs}}(\lambda) \cdot \eta_{\mathrm{Diff}}(\lambda) \cdot \eta_{\mathrm{Diss}} \cdot \eta_{\mathrm{CC}} \tag{S5}$$

where η_{Abs}, η_{Diff}, η_{Diss}, and η_{CC} correspond to the active layer photon absorption, exciton diffusion, exciton dissociation, and charge collection efficiencies, respectively.[10] Due to the dispersion of refractive indices and coherent optical interference within the device, both η_{Abs} and η_{Diff} are wavelength-dependent. η_{Diss} depends on the polaron pair kinetics at the heterojunction and η_{CC} depends on transport of free charges to their respective electrodes, making both η_{Diss} and η_{CC} wavelength independent.

It can also be helpful to separate changes in absorption from other processes comprising EQE by defining the IQE as:

$$\eta_{\mathrm{IQE}}(\lambda) = \frac{\eta_{\mathrm{EQE}}(\lambda)}{\eta_{\mathrm{Abs}}(\lambda)} \tag{S6}$$

which describes the efficiency of converting photogenerated excitons into electrical current.

During operation at zero applied bias (Figure 2c), both subjunctions act as current sources operating electrically in parallel with a barrier-free extraction of charge carriers upon exciton dissociation.[11] Since each subjunction's photocurrent is additive, the net EQE for a CHJ can be written as:

$$\mathrm{EQE}(\lambda) = \eta_{\mathrm{Abs}}(\lambda) \cdot \sum_{i=1}^{\mathrm{N}} \eta_{\mathrm{Diff,i}}(\lambda) \cdot \eta_{\mathrm{Diss,i}} \cdot \eta_{\mathrm{CC,i}} \tag{S7}$$

where N is the number of subjunctions in the CHJ device. In the interlayer, there will be a η_{Diff} for excitons diffusing to the EDL/interlayer heterojunction and a separate η_{Diff} for those reaching the interlayer/acceptor heterojunction. Because there is a heterojunction on both sides of the interlayer, the net η_{Diff} of the interlayer in the CHJ device will be significantly higher than the η_{Diff} of that same layer in a SHJ configuration, due to the decreased distance excitons nearest the anode must travel before being dissociated.

4. *J-V* Curves of CHJ Devices

Figure S7a and Figure S7b show the experimentally determined *J-V* curves (CHJ and SHJs corresponding to each subjunction) for the TcTa/SubPc/C_{60} and BPAPF/SubNc/C_{60} systems, respectively. **Table S2** and **Table S3** provide tabulated *J-V* performance parameters for all SHJs (EDL/interlayer and interlayer/C_{60}) and all CHJs (5 nm EDL/interlayer/C_{60}) used in this study. Even with a nominal ΔE_{HOMO} = 0.02 eV, as is the case with the BPAPF/SubNc heterojunction, there can still be efficient dissociation of excitons (and photocurrent production) at short-circuit conditions.

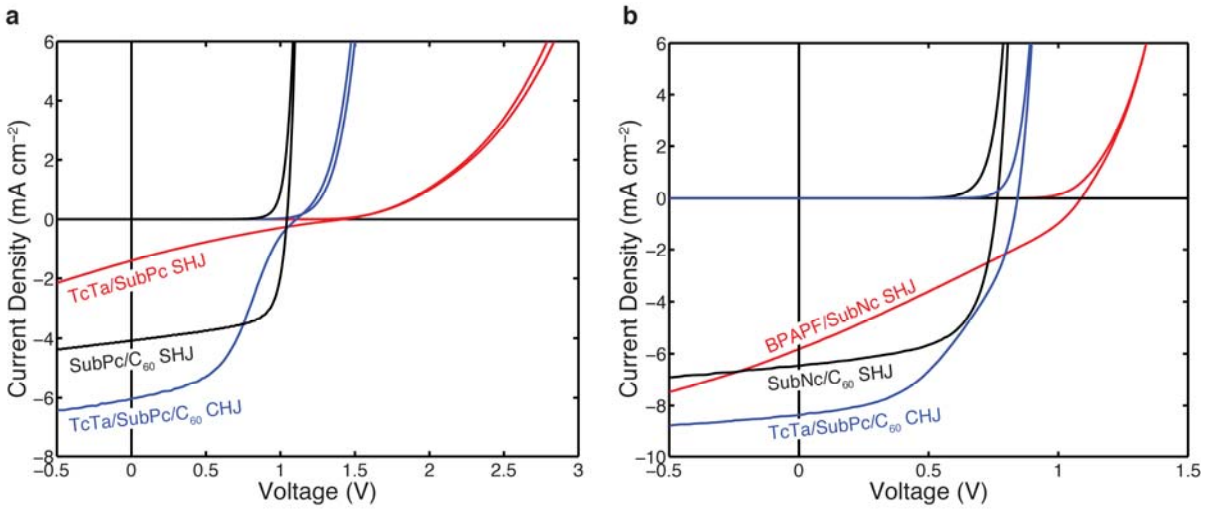

Figure S7. *J-V* curves for a) TcTa/SubPc SHJ, SubPc/C_{60} SHJ, and TcTa/SubPc/C_{60} CHJ devices; and b) BPAPF/SubNc SHJ, SubNc/C_{60} SHJ, and BPAPF/SubNc/C_{60} CHJ devices.

Table S2. Performance parameters for SHJ and CHJ devices utilizing SubPc in this study. Standard deviations, as calculated from at least six different devices, for V_{oc}, J_{sc}, FF, PCE, and V_{MPP} were all less than 3%, 11%, 6%, 12%, and 4%, respectively.

Device	ΔE_{HOMO} [eV]	V_{oc} [V]	J_{sc} [mA cm^{-2}]	FF [%]	PCE [%]	V_{MPP} [V]
SubPc/C_{60} SHJ	-	1.04	3.9	67	2.74	0.89
TcTa/SubPc SHJ	0.05	1.41	1.5	21	0.44	0.63
TcTa/SubPc/C_{60} CHJ		1.11	5.8	44	2.81	0.63
BPAPF/SubPc SHJ	0.17	1.42	1.3	20	0.38	0.63
BPAPF/SubPc/C_{60} CHJ		1.15	5.7	41	2.70	0.61
α-NPD/SubPc SHJ	0.20	1.35	1.9	23	0.60	0.65
α-NPD/SubPc/C_{60} CHJ		1.13	5.7	43	2.76	0.63
HMTPD/SubPc SHJ	0.23	1.38	1.4	21	0.40	0.62
HMTPD/SubPc/C_{60} CHJ		1.11	5.7	42	2.69	0.62
TPTPA/SubPc SHJ	0.27	1.33	3.1	38	1.58	0.82
TPTPA/SubPc/C_{60} CHJ		1.03	5.3	51	2.79	0.68
TAPC/SubPc SHJ	0.34	1.30	1.9	27	0.65	0.69
TAPC/SubPc/C_{60} CHJ		1.10	5.8	38	2.42	0.55
NPB/SubPc/SHJ	0.35	1.32	1.9	28	0.71	0.71
NPB/SubPc/C_{60} CHJ		1.12	6.0	38	2.60	0.57
TPD/SubPc SHJ	0.38	1.26	2.0	30	0.77	0.72
TPD/SubPc/C_{60} CHJ		1.08	5.8	36	2.25	0.52
DMFL-NPB/SubPc SHJ	0.48	1.17	1.9	31	0.65	0.64
DMFL-NPB/SubPc/C_{60} CHJ		0.97	5.6	34	1.85	0.46
MeO-TPD/SubPc SHJ	0.55	1.14	1.6	34	0.62	0.69
MeO-TPD/SubPc/C_{60} CHJ		0.93	5.1	39	1.86	0.49
m-MTDATA/SubPc SHJ	0.62	1.08	1.2	24	0.33	0.51
m-MTDATA/SubPc/C_{60} CHJ		0.79	4.4	23	0.80	0.30
2T-NATA/SubPc SHJ	0.65	1.07	2.0	33	0.70	0.62
2T-NATA/SubPc/C_{60} CHJ		0.89	5.2	28	1.31	0.35

Table S3. Performance parameters for SHJ and CHJ devices using SubNc in this study. Standard deviations, as calculated from at least six different devices, for V_{oc}, J_{sc}, FF, PCE, and V_{MPP} were all less than 2%, 9%, 7%, 10%, and 3%, respectively.

Device	ΔE_{HOMO} [eV]	V_{oc} [V]	J_{sc} [mA cm^{-2}]	FF [%]	PCE [%]	V_{MPP} [V]
SubNc/C_{60} SHJ	-	0.75	5.9	62	2.76	0.59
BPAPF/SubNc SHJ	0.02	1.08	5.1	30	1.64	0.62
BPAPF/SubNc/C_{60} CHJ		0.84	8.0	47	3.18	0.54
α-NPD/SubNc SHJ	0.05	1.08	4.7	29	1.50	0.60
α-NPD/SubNc/C_{60} CHJ		0.86	8.0	53	3.59	0.59
TPTPA/SubNc SHJ	0.12	1.09	5.1	29	1.63	0.60
TPTPA/SubNc/C_{60} CHJ		0.86	8.2	51	3.65	0.57
TAPC/SubNc SHJ	0.19	1.11	5.2	30	1.73	0.63
TAPC/SubNc/C_{60} CHJ		0.85	8.3	58	4.05	0.60
NPB/SubNc/SHJ	0.20	1.11	5.6	34	2.10	0.67
NPB/SubNc/C_{60} CHJ		0.84	8.2	50	3.46	0.54
TPD/SubNc SHJ	0.23	1.00	1.9	25	0.48	0.51
TPD/SubNc/C_{60} CHJ		0.86	7.2	44	2.70	0.52
DMFL-NPB/SubNc SHJ	0.33	1.05	4.0	29	1.21	0.60
DMFL-NPB/SubNc/C_{60} CHJ		0.87	7.9	41	2.79	0.49
MeO-TPD/SubNc SHJ	0.40	1.04	3.1	28	0.93	0.57
MeO-TPD/SubNc/C_{60} CHJ		0.91	7.4	33	2.21	0.45
m-MTDATA/SubNc SHJ	0.47	1.06	4.9	32	1.63	0.63
m-MTDATA/SubNc/C_{60} CHJ		0.91	8.2	23	1.74	0.38
2T-NATA/SubNc SHJ	0.50	0.94	1.8	27	0.44	0.51
2T-NATA/SubNc/C_{60} CHJ		0.77	5.2	28	1.12	0.38

[1] B. Verreet, S. Schols, D. Cheyns, B. P. Rand, H. Gommans, T. Aernouts, P. Heremans, J. Genoe, Journal of Materials Chemistry 2009, 19, 5295.
[2] C. L. Braun, The Journal of Chemical Physics 1984, 80, 4157; L. Onsager, Physical Review 1938, 54, 554.
[3] C. K. Renshaw, J. D. Zimmerman, B. E. Lassiter, S. R. Forrest, Physical Review B 2012, 86.
[4] N. C. Giebink, G. P. Wiederrecht, M. R. Wasielewski, S. R. Forrest, Physical Review B 2010, 82.
[5] S. Noh, C. K. Suman, Y. Hong, C. Lee, Journal of Applied Physics 2009, 105, 033709.
[6] A. Fleissner, H. Schmid, C. Melzer, H. von Seggern, Applied Physics Letters 2007, 91, 242103.
[7] H. Kageyama, H. Ohishi, M. Tanaka, Y. Ohmori, Y. Shirota, Advanced Functional Materials 2009, 19, 3948.
[8] P. M. Borsenberger, L. Pautmeier, R. Richert, H. Bässler, The Journal of Chemical Physics 1991, 94, 8276.
[9] J. Frenkel, Physical Review 1938, 54, 647; P. W. M. Blom, M. J. M. de Jong, M. G. van Munster, Physical Review B 1997, 55, R656; S. V. Rakhmanova, E. M. Conwell, Applied Physics Letters 2000, 76, 3822.
[10] B. A. Gregg, The Journal of Physical Chemistry B 2003, 107, 4688.
[11] A. Barito, M. E. Sykes, D. Bilby, J. Amonoo, Y. Jin, S. E. Morris, P. F. Green, J. Kim, M. Shtein, Journal of Applied Physics 2013, 113, 203110.